JOURNAL OF AIRCRAFT
Vol. 44, No. 3, May–June 2007

Local and Total Density Measurements in Ice Shapes

Mario Vargas*
NASA Glenn Research Center, Brook Park, Ohio 44135
Howard Broughton†
Pace Levy Inc., Westlake, Ohio 44145
James J. Sims‡
Universal Imaging Corporation, Downingtown, Pennsylvania 19335
Brian Bleeze§
ISPA Technology, Inc., Alexandria, Virginia 22314
and
Vatanna Gaines¶
Lockheed Martin Aeronautics Company, Marietta, Georgia 30063

DOI: 10.2514/1.23326

Preliminary measurements of local and total densities inside ice shapes were obtained from ice shapes grown in the NASA John H. Glenn Icing Research Tunnel for a range of glaze ice, rime ice, and mixed-phase ice conditions on a NACA 0012 airfoil at 0-deg angle of attack. Prodi's x-ray contact microradiography method was extended using modern imaging techniques to conduct the measurements. The ice shapes were removed from the airfoil and a slice of ice 3-mm thick was obtained using a microtome. The resulting samples were then x-rayed to obtain a microradiograph, the film was digitized, and image processing techniques were used to extract the local and total density values.

Nomenclature

D = photographic density of the film
D_A = photographic density of the film after exposure to the transmitted beam intensity through the ice region free of voids
D_B = photographic density of the film after exposure to the transmitted beam intensity through the ice sample
Do = photographic density of the film after direct exposure to the beam intensity I_o
D_R = photographic density of the film after exposure to the transmitted beam intensity through the reference piece
E = photographic exposure
I = beam intensity
I_A = transmitted intensity of the x-ray beam through the ice region free of voids
I_B = transmitted intensity of the x-ray beam through the ice sample
I_o = intensity of the parallel monochromatic x-ray beam
m_B = mass contained in volume X_A.1.1 in the area of the ice with voids
t = time of exposure to transmitted intensity
X = thickness of the material
X_A = thickness of the ice in the region free of voids
X_B = true thickness of the ice sample (thickness less voids)
X_R = thickness of the reference piece
γ = slope of the straight line part of the characteristic curve of the photographic emulsion
ρ_H = density of the ice sample
ρ_I = density of the ice in the region free of voids
σ = absorption coefficient

Presented as Paper 0657 at the 43rd AIAA Aerospace Sciences Meeting and Exhibit, Reno, NV, 10–13 January 2005; received 19 February 2006; revision received 5 July 2006; accepted for publication 7 July 2006.

*Aerospace Engineer, Icing Branch, 21000 Brookpark Road. Member AIAA.
†President, P.O. Box 450648.
‡North American Sales, 402 Boot Road.
§Managing Partner, 129 South Fairfax Street.
¶Aeronautical Engineer Senior, F/A-22 Structures Analysis and Integration Team, 86 South Cobb Drive.

I. Introduction

PART of the aircraft icing research program at NASA John H. Glenn Research Center involves the study and measurement of local and total densities of ice shapes accreted on airfoils. Local density is measured at a given location inside a slice taken from the ice shape. Total density is calculated for the whole slice. Density measurements are needed to study the structure and formation of ice and to obtain fundamental data for the density correlations employed in computer codes that model ice accretion.

This report presents the results of a preliminary experiment carried out in the Icing Research Tunnel (IRT) at NASA John H. Glenn Research Center to measure the local and total densities of ice shapes accreted on a NACA 0012 airfoil mounted vertically at a 0-deg angle of attack. Density measurements were performed using Prodi's [1,2] x-ray contact microradiography method (of measuring ice density). In the past, measurements of accreted ice density have mainly been performed by using the rotating multicylinder technique [3,4], but there are difficulties in extending the results to nonrotating bodies such as airfoils [5]. Prodi's technique was chosen because it allows the measurement of local and total densities inside ice shapes accreted on an airfoil. Prodi's technique, originally applied to hailstones, was extended by taking advantage of modern imaging techniques to measure local and total densities in ice shapes accreted on a NACA 0012 airfoil for a range of icing conditions.

Results are presented for the rime, mixed, and glaze ice cases. For each ice sample, local densities were measured across different regions of the ice shape. Total densities were also measured for each sample. In addition to the density measurements, image processing techniques were used to visualize air pockets present inside the ice shapes.

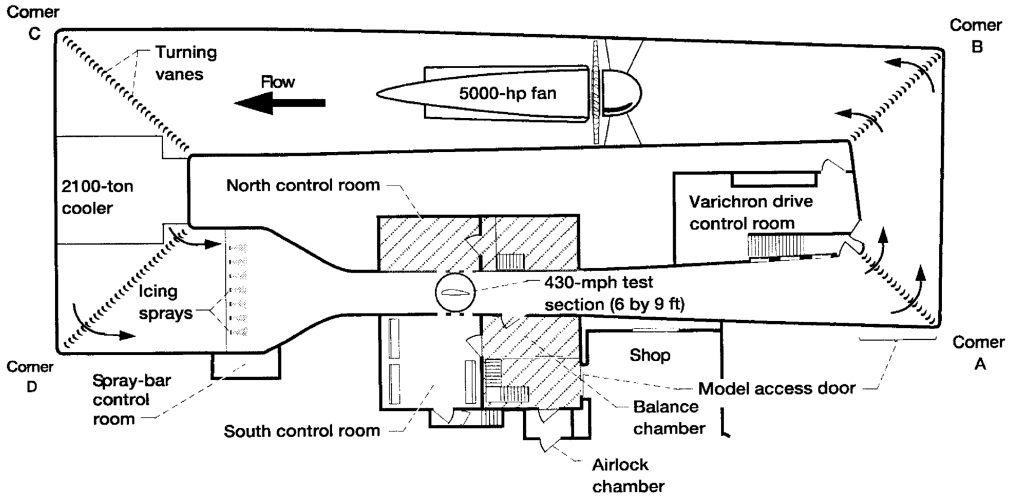

Fig. 1 NASA John H. Glenn Icing Research Tunnel, plan view.

II. Description of Experiment

A. NASA John H. Glenn Icing Research Tunnel

Figure 1 shows the Icing Research Tunnel [6]. The IRT is a closed-loop, refrigerated wind tunnel with a test section 6-ft high, 9-ft wide, and 20-ft long. The temperature in the test section can be controlled from −20 to +33°F. Velocities up to 350 mph can be obtained. A spray system allows control of the liquid water content (LWC) between 0.5 to 2.5 g/m^3. The spray nozzles provide droplet median volume diameters (MVD) from 14 to 50 μm.

B. Test Hardware

The ice shapes were accreted on a 21-in.-chord NACA 0012 airfoil mounted vertically in the test section. The angle of attack was set to 0 deg. An electric heater system consisting of the heater and a power supply allowed the removal of the ice shapes. Figure 2 shows the airfoil in the test section with the electric heater mounted in the center.

A Puffer Hubbard freezer was employed to store the ice shapes. The freezer temperature could be controlled between 0 and −35°F. The samples were stored at −15°F.

A Zeiss HM 400R sliding microtome with a C profile steel knife was employed to shave the ice samples to a thickness of 3 mm. The microtome had a fine control from 0 to 60 μm, which allowed the removal of the ice in small increments from the initial 10-mm samples cut with the saw. Figure 3 shows the microtome.

A Watkins–Johnson x-ray source (type WJ-2308-2 Dmo) was used to x-ray the samples. The x-ray unit was mounted on a modified photographic enlarger. The unit had a maximum voltage of 50 kV, a maximum output power of 50 W, and a maximum current of 100 mA. For safety reasons, the x-ray device was shielded on three sides with 1/4-in.-thick aluminum plates to block scattered rays. Figure 4 shows the x-ray source.

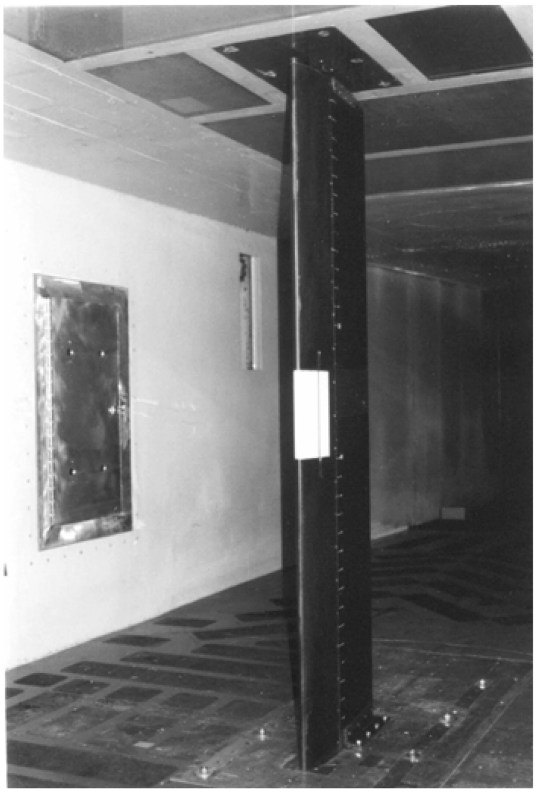

Fig. 2 NACA 0012 airfoil at a 0-deg angle of attack, positioned for testing in the IRT. The white patch in the center of the airfoil is the electric heater.

C. Test Conditions

The test conditions were selected to obtain accretions of rime ice, mixed ice, and glaze ice. Test conditions are listed in Table 1. Settings for the x-ray source are listed in Table 2.

D. Test Procedure

Ice shapes were accreted on the NACA 0012 airfoil in the IRT for the icing conditions listed in Table 1. Figure 5 shows a schematic of

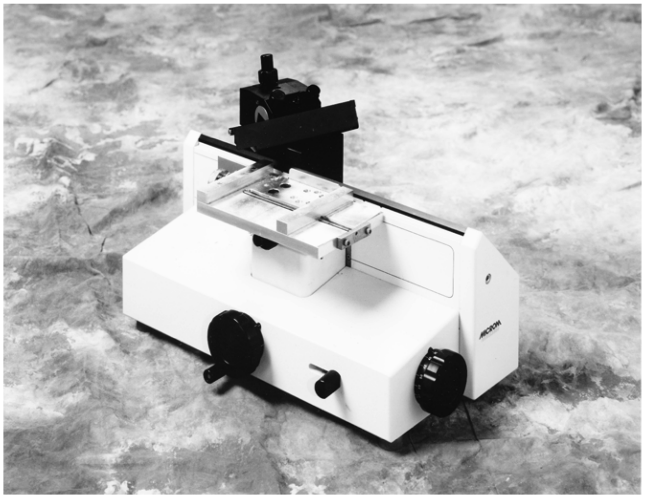

Fig. 3 Sliding microtome.

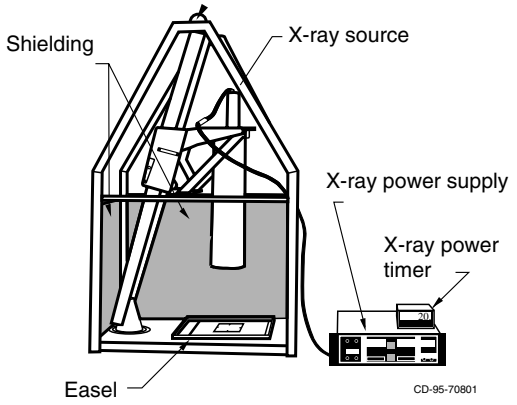

Fig. 4 X-ray device.

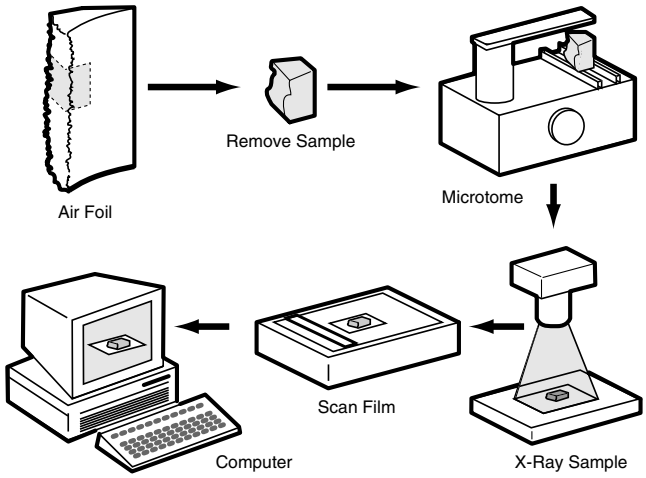

Fig. 5 Methodology of the experiment.

the experimental methodology. An aluminum block with the indented profile of the airfoil geometry was used to make three cuts in the ice in the region of the heater: one at each end of the heater and another at the midpoint. The heater was activated and the two ice shapes were removed and wrapped in polyvinyl film. The wrapping technique consisted of placing the ice shape in the middle of a piece of polyvinyl film, enveloping the film all around the ice shape, removing as much air as possible by suction, and closing the plastic with a twist-on tie. The ice shapes were stored in the freezer at −15°F.

When the needed ice samples were collected, the temperature of the tunnel was lowered to 0°F, the airflow was stopped, and the tunnel was used as a cold room. The experimental hardware was moved inside the tunnel and allowed to chill until it reached ambient temperature. The ice samples were then removed from the freezer and cut to approximately 10-mm thickness with a band saw.

Table 2 X-ray settings; setting 2 was used on some samples to reduce vibration effects.

	Setting 1	Setting 2
Voltage	25 kV	30 kV
Current	100 mA	100 mA
Distance from x-ray source to ice sample	2 ft	2 ft
Time of exposure	50 s	35 s

To mount the thick slices onto the microtome, an aluminum plate with a trace amount of water frozen on it was placed on a heating pad. When the plate reached the temperature at which the trace quantity of ice was beginning to melt, the plate was removed from the heating pad and the sample placed on it. The plate was immediately placed on a large steel block that acted as a cold sink. The thin liquid film that developed between the ice sample and the plate froze immediately, creating a very strong bond. Extreme care was exercised to keep the thin film to a minimum, to avoid contamination of the sample.

One side of the sample was microtomed, creating a flat surface, then the sample was removed from the plate, flipped over, refrozen to the plate, and the reverse side was microtomed. Because the mounting plate was adjusted to be parallel to the cutting blade, the top and bottom surfaces of the ice sample were also nearly parallel. As the sample neared 3 mm in thickness, it was measured at eight locations around the perimeter with a depth gage. Microtoming continued until the desired thickness was obtained.

Once the sample was determined to be 3-mm thick, it was removed from the mounting block. The instant that the sample became free from the block, it was carefully placed on a sheet of Mylar used to transfer it to the x-ray source. The Watkins–Johnson x-ray source was used to x-ray the sample. Kodak Industrex Ready Pack II type M x-ray film was used because of its high resolution and sealed packaging. The film was held in place by the film holder (a modified easel), and the sample was placed in contact with the film packet. Before exposure, the x-ray device was run for several minutes to warm up and reach a stable operational mode. Exposure was determined in the pretest phase of the experiment, ensuring that the density of the film was within the dynamic range of the film scanner to be used in the image processing and that the exposure was within the linear part of the characteristic curve of the film emulsion. An input current of 1 mA and 25 kV, exposing the film for 50 s, produced sufficient density. An exposure of 1 mA and 20 kV for 35 s was used on some samples, to reduce vibration effects.

E. Image Processing

Processing of the film was performed with a Kodak X-Omat radiographic film processor at the recommended time and temperature. The radiographs were scanned with a Leafscan-45 film scanner at a resolution of 1100 pixels per inch (ppi) and saved to a file. Before the experiment, the film scanner was tested to evaluate its consistency from scan to scan. It was found that the scanner

Table 1 Test conditions

Figure in the paper	Image	Run no.	Velocity, mph	LWC, g/m^3	MVD, μm	Temperature °F	Spray time, min	Ice type
	$SAG_{2cFF.TIF}$	061394.01	150	0.5	20	28	12	glaze
Figure 9	$SAH_{2cFF.TIF}$	061394.02	150	0.75	20	28	12	glaze
Figure 8	$SAI_{1cFF.TIF}$	061394.03	150	1.0	20	28	12	glaze
Figure 10	$SAO_{1cFF.TIF}$	061394.01	150	1.25	20	28	12	glaze
	$SAM_{1cFF.TIF}$	061594.04	150	1.0	20	28	6	glaze
Figure 11	$SAL_{1cFF.TIF}$	061594.01	100	1.0	20	28	12	glaze
Figure 12	$SR_{1cFF.TIF}$	062194.01	150	1.0	30	12	12	glaze
Figure 13	$SAJ_{1cFF.TIF}$	061394.06	150	1.0	20	12	12	mixed
	$SL_{1cFF.TIF}$	061594.09	150	1.0	20	12	12	mixed
Figure 14	$SO_{1cFF.TIF}$	061594.08	150	0.75	20	12	12	mixed
	$SN_{2cFF.TIF}$	061594.10	150	1.25	20	12	12	mixed
	$SS_{1cFF.TIF}$	062194.02	150	1.0	20	12	6	mixed
Figure 15	$SZ_{1cFF.TIF}$	062194.09	150	1.0	30	0	12	mixed
Figure 16	$SAA_{2cFF.TIF}$	062194.10	100	1.0	20	0	12	rime
Figure 17	$SAB_{1cFF.TIF}$	062194.11	200	1.0	20	0	12	rime

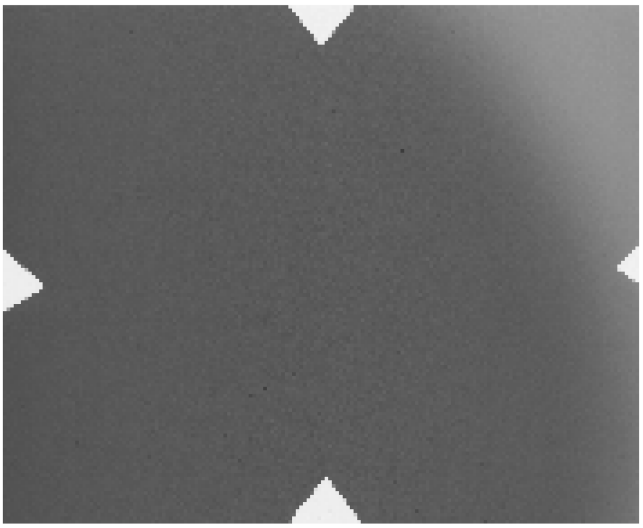

Fig. 6 Flat-field image with triangular registration marks used to verify alignment when superimposing flat-field images and sample images.

autoranged the output gray values based on the radiograph density range. The autoranging changed the internal lookup table based on the minimum and maximum intensity value of the prescanned image, thereby expanding the dynamic range of the output image. To circumvent the autoranging feature, a balanced target was prescanned (in this case, Kodak gray scale), which provided the same minimum and maximum intensity value for each subsequent scan.

Nonuniformities in the x-ray source caused density variations in the film that would affect the localized density measurements. To compensate, a series of flat-field images were exposed each day of the experiment. Each flat-field image was exposed under the x-ray source without a sample. The flat-field images were added to obtain an average flat-field image that was digitally subtracted from the sample images.

To accurately add the flat-field images and subtract the average from the sample images, registration of the images had to be performed for proper alignment. This was done using two of the four V-shaped registration marks (see Fig. 6) that were exposed on each sheet of film to facilitate registration of each image. By having several registration marks, any two (or all) could be used to insure registration accuracy.

Each registration mark was enlarged sufficiently to locate the end point. This was determined accurately by counting the cross-sectional profile of pixels across the registration point and selecting the midpoint pixel, then counting the pixels from the edge of the film to the same midpoint pixel, and using these values as a standard measurement for the entire experiment.

To register one image to another, they were superimposed so that each midpoint pixel resided at the same spatial location. The displacement of opposite registration marks was checked to verify proper alignment when scanned. If this varied by more than five pixels, then the radiograph was realigned in the film holder and rescanned. Other point-to-point calculations were used to monitor shrinkage and swelling of the film, which was found to be negligible.

Once all the radiographs were scanned and registered, the flat-field images for that particular day were averaged together into a single flat-field image $g(x, y)$:

$$g(x,y) = \frac{1}{N}\sum_{i=1}^{N} fd_i(x,y) \tag{1}$$

where $fd_i(x, y)$ is each flat-field image. The averaged flat-field image was then subtracted from all of the samples images $s(x, y)$, which resulted in the sample image $fs(x, y)$ with corrected intensity values:

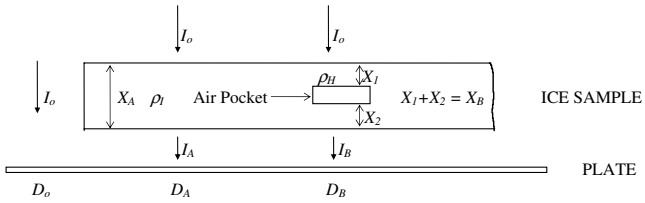

Fig. 7 Nomenclature used to describe the absorption of a parallel monochromatic x-ray beam of intensity *Io* incident on the ice sample and on the plate; adapted from Prodi [1].

$$fs(x,y) = s(x,y) - g(x,y) \tag{2}$$

Data analysis based on Prodi's methodology was used on image $fs(x, y)$ to obtain the physical densities.

F. Prodi's Methodology

Correlation of the density (blackness) of the film with the actual physical density of the ice sample is based on Prodi's methodology. The following description of the methodology closely follows Prodi's [1,2], with some added comments about the assumptions implied in the methodology.

Assume a parallel monochromatic x-ray beam of intensity I_o incident on the ice sample and on the thin plate (see Fig. 7). X_A is the thickness of the region of the ice free of voids (air bubbles), ρ_I the density of the ice in this region, I_A the transmitted intensity, and D_A the density of the film due to the exposure to the transmitted intensity.

In a region of the ice containing air bubbles, X_A is still the thickness of the ice sample (sample assumed to have parallel faces), X_B is the true thickness of the material (thickness of the material less voids), ρ_H the density of the ice in this region, I_B the transmitted intensity, and D_B the density of the film due to the exposure to the transmitted intensity.

The ratio of the density of ice in a region containing air bubbles to the density of ice in a region free of air bubbles can be related to the ratio of the true thickness of the two regions:

$$m_B = \rho_H X_A \tag{3}$$

where m_B can be expressed as

$$m_B = \rho_I X_B \tag{4}$$

then

$$\rho_H X_A = \rho_I X_B \tag{5}$$

and

$$\rho_H/\rho_I = X_B/X_A \tag{6}$$

The assumption to obtain Eq. (6) is that the faces of the sample in the region of ice without air bubbles and in the ice with bubbles have the same thickness. A more subtle assumption is that the solid ice between the bubbles in region B is of the same type as the ice without bubbles in region A. This seemingly trivial fact has special significance in icing: the ice without bubbles is glaze ice and the ice with bubbles is rime or mixed ice. The physics of the formation of the two kinds of ice are different, and there is no a priori reason why the two kinds of ice have to be equal. Another important assumption in the preceding derivation and in the next step is that the beam is monochromatic.

The ratio of the true thickness X_B/X_A can be related to the beam intensity using Lambert's law:

$$I = I_o \exp(-\sigma X) \tag{7}$$

where I_o and I are the incident and transmitted radiation, respectively.

From Eq. (7)

$$X = (1/\sigma)\,\ell_n(I_o/I) \tag{8}$$

and

$$X_B/X_A = \ell_n(I_o/I_B)/\ \ell_n(I_o/I_A) \tag{9}$$

where the coefficient of absorption has been canceled out, assuming the ice is homogeneous wherever there are no bubbles.

Substitution of Eq. (6) into Eq. (9) gives

$$\rho_H/\rho_I = \ell_n(I_o/I_B)/\ \ell_n(I_o/I_A) \tag{10}$$

Photographic exposure E can be expressed as

$$E = I \cdot t \tag{11}$$

The slope of the straight line part of the characteristic curve of the photographic emulsion is defined as

$$\gamma = D/\log(E) = D/\log(I \cdot t) = D/(\log I + \log t) \tag{12}$$

where

$$\log(I) = [D - \gamma \cdot \log(t)]/\gamma \tag{13}$$

If we operate in the linear region of the film in which γ is constant, then:

$$\rho_H/\rho_I = \{[(D_o - \gamma \cdot \log t)/\gamma] - [(D_B - \gamma \cdot \log t)/\gamma]\}/\{[(D_o - \gamma \cdot \log t)/\gamma] - [(D_A - \gamma \cdot \log t)/\gamma]\} \tag{14}$$

then

$$\rho_H/\rho_I = X_B/X_A = (D_o - D_B)/(D_o - D_A) \tag{15}$$

The local density of the ice sample in a given location can be obtained if we know the density at a location within the sample in which the ice is clear of bubbles and if we measure the film density at three locations: in a region in which the ice is clear of bubbles, in a region of the film away from the sample, and in the region in which we want to measure the physical density of the ice:

$$\rho_H = \rho_I(D_o - D_B)/(D_o - D_A) \tag{16}$$

III. Data Analysis

A. Local Density

Once the film was scanned and the information was in files, each image was first analyzed using an image processing program (Adobe Photoshop [7]) to locate a reference area (about 1×2 mm) of clear ice in which no air pockets were visible and for which the thickness was 3 mm. Once this area was located, the average gray value for the area was obtained and the gray value was assigned to D_A in Eq. (16). The physical density value for this reference area, ρ_I in Eq. (16), was assumed to be 0.917 g/cm^3, the typical density of clear ice. A more accurate approach (not used in this experiment) using a separate reference ice piece is discussed in the Appendix. The gray level of the field surrounding the ice sample was expected to be zero, due to the flat-field subtraction. When the gray levels for the surrounding field were measured, they exhibited small deviations from zero. We used D_o equal to zero in Eq. (16) and assumed the small deviation from zero to be part of the error in the measurement.

Next, the images were analyzed with a separate image processing application (Sigma Scan [8]) to extract intensity profile data. The gray value intensity across various profiles on areas of interest was recorded in a spreadsheet (Excel [9]). The gray levels were then converted to local ice densities using Eq. (16), and the results were plotted for each image.

B. Total Density

The total density for each image was also calculated in the following way: Adobe Photoshop was used to obtain the mean gray value for the whole image; this value was assigned to D_B. D_A, D_o, and ρ_I were obtained as in the case of the local densities. Equation (16) was then used to calculate ρ_H, which was now taken as the total density for the sample.

To visualize the air pockets observed in the samples, edge detection with thresholding was applied to the images using Adobe Photoshop.

IV. Results

A. Glaze Ice Cases

To study the density in glaze ice shapes, a baseline case was chosen ($V = 150$ mph, LWC $= 1.0$ g/m^3, MVD $= 20$ mm, $T_{\text{tot}} = 28°$F, and $\tau = 12$ min) and other cases were obtained by changing one or two of the conditions with respect to the base case. The LWC was varied from 0.5 to 1.25 g/cm^3 at 0.25 g/cm^3 increments. Figures 8–10 show the results for a LWC of 1.0, 0.75, and 1.25 g/cm^3. For each case, the local densities were measured along two straight lines labeled Red and Green. The local densities values tend to remain close to 0.917 g/cm^3, changing dramatically only when there is a void (bubble or air pocket) in the ice. The small deviations observed in the local density values are attributed to the effect of nonuniformities in the x-ray beam, because the flat-field subtraction technique does not eliminate all the nonuniformities and the ice sample has some variations in thickness. Similar results were observed when the velocity was decreased to 100 mph (Fig. 11); when the temperature was decreased to 12°F while the MVD was simultaneously increased to 30 μm (Fig. 12); and when the ice accretion time was decreased from 12 to 6 min (no figure provided).

B. Mixed Ice Cases

The case shown in Fig. 13 ($V = 150$ mph, LWC $= 1.0$ g/m^3, MVD $= 20$ μm, $T_{\text{tot}} = 12°$F, and $\tau = 12$ min) was chosen as the base case for the mixed ice cases, and other cases were obtained by

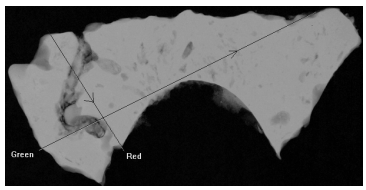

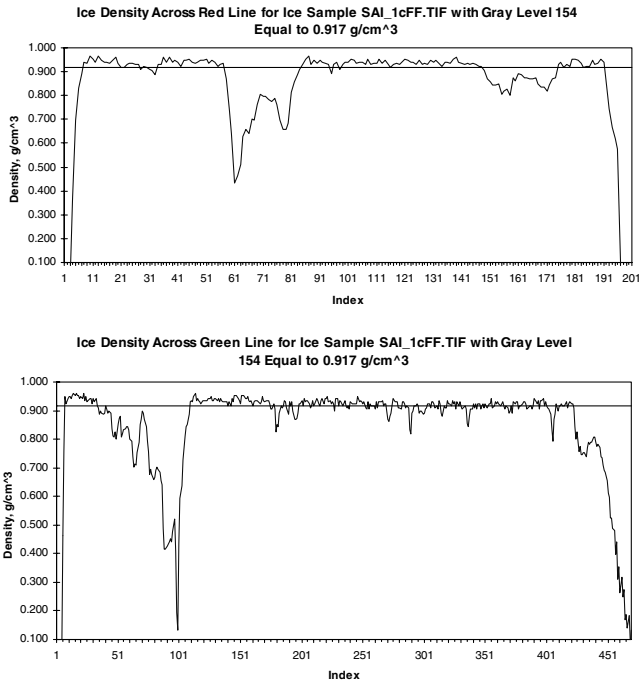

Fig. 8 Sample $\text{SAI}_{\text{1cFF.TIF}}$ for the glaze ice case; $V = 150$ mph, LWC $= 1.0$ g/m^3, MVD $= 20$ μm, $T_{\text{tot}} = 28°$F, and $\tau = 12$ min.

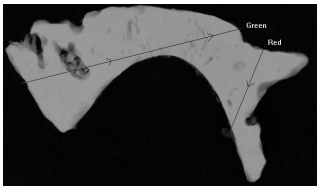

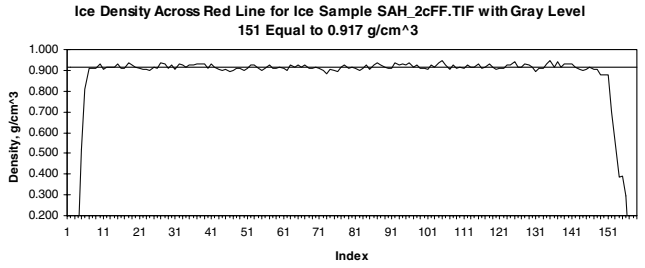

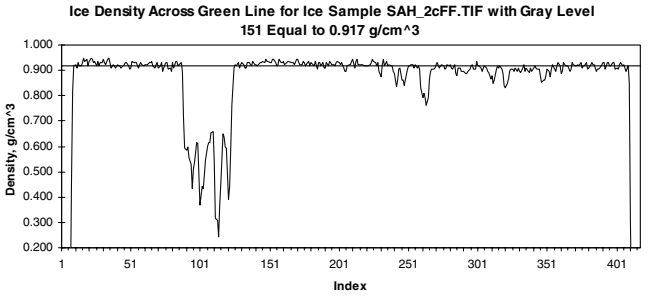

Fig. 9 Sample $\mathrm{SAH}_{\mathrm{2cFF.TIF}}$ for the glaze ice case; $V = 150$ mph, LWC $= 0.75$ g/m^3, MVD $= 20$ μm, $T_{\mathrm{tot}} = 28°$F, and $\tau = 12$ min.

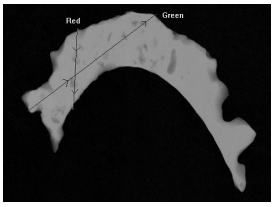

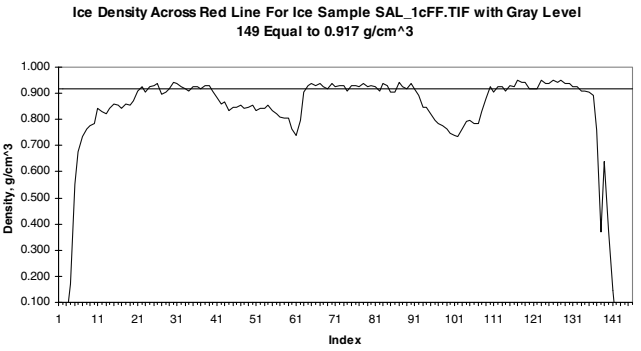

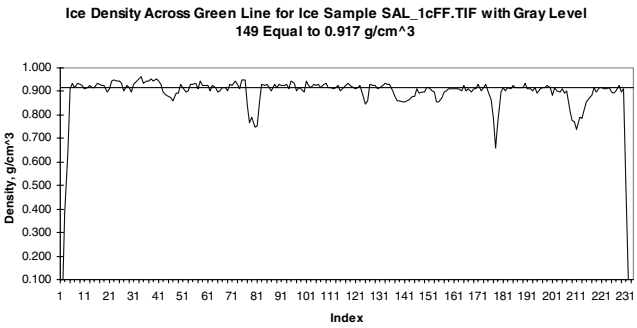

Fig. 11 Sample $\mathrm{SAL}_{\mathrm{1cFF.TIF}}$ for the glaze ice case; $V = 100$ mph, LWC $= 1.0$ g/m^3, MVD $= 20$ μm, $T_{\mathrm{tot}} = 28°$F, and $\tau = 12$ min.

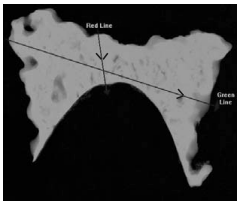

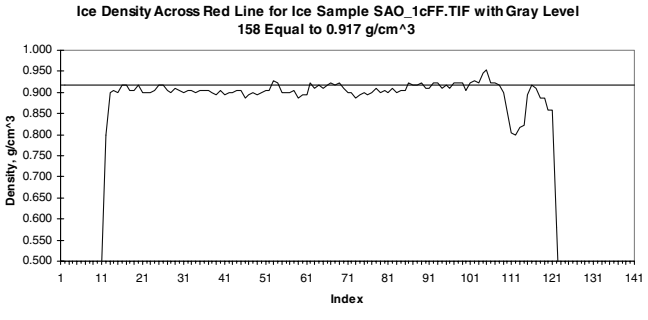

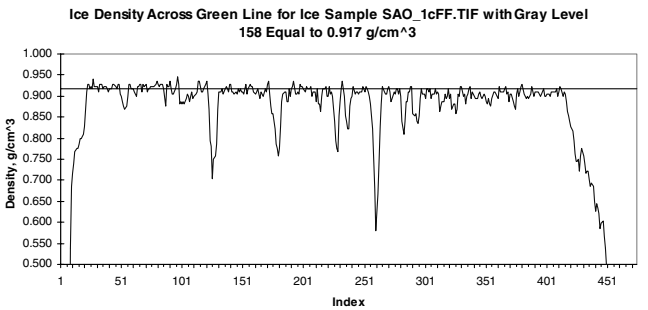

Fig. 10 Sample $\mathrm{SAO}_{\mathrm{1cFF.TIF}}$ for the glaze ice case; $V = 150$ mph, LWC $= 1.25$ g/m^3, MVD $= 20$ μm, $T_{\mathrm{tot}} = 28°$F, and $\tau = 12$ min.

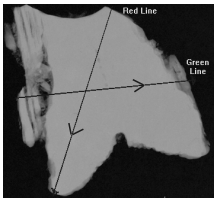

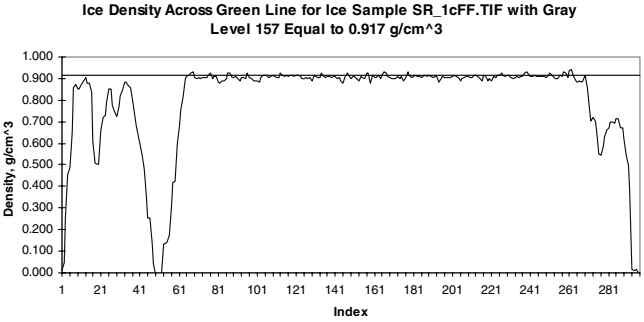

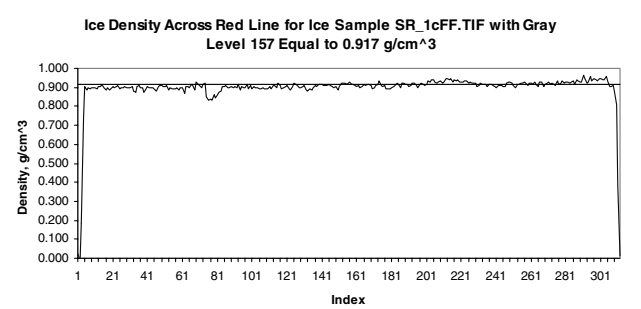

Fig. 12 Sample $\mathrm{SR}_{\mathrm{1cFF.TIF}}$ for the glaze ice case; $V = 150$ mph, LWC $= 1.0$ g/m^3, MVD $= 30$ μm, $T_{\mathrm{tot}} = 12°$F, and $\tau = 12$ min.

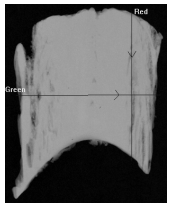

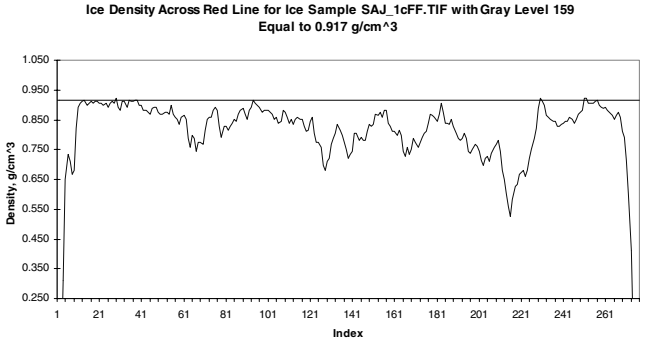

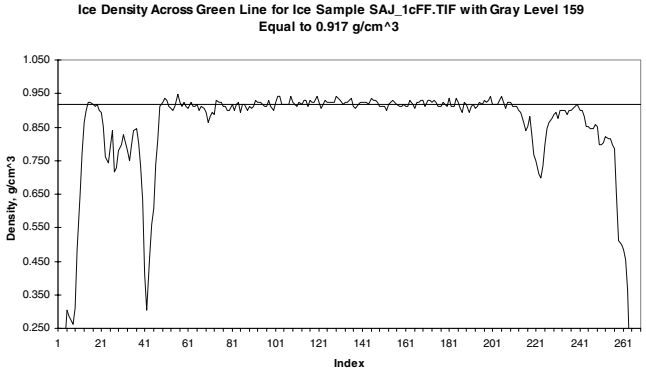

Fig. 13 Sample $SAJ_{1cFF.TIF}$ for the mixed ice case; $V = 150$ mph, LWC $= 1.0$ g/m^3, MVD $= 20$ μm, $T_{tot} = 12°$F, and $\tau = 12$ min.

changing one of the conditions with respect to the base case. The LWC was varied from 0.75 to 1.25 g/cm^3 at 0.25 g/cm^3 increments. Figure 14 shows the result for a LWC of 0.75 g/cm^3. One case was done in which the temperature was decreased to 0°F while the MVD was simultaneously increased to 30 μm. This case is presented in Fig. 15. The trend in all the mixed ice cases follows the results for the glaze ice cases: the densities measured along the two lines labeled Green and Red tend to remain near 0.917 g/cm^3, with small deviations due to nonuniformities in the x-ray beam and the thickness of the ice sample, and with large changes in the densities due to air pockets in the ice.

C. Rime Ice Cases

Figures 16 and 17 present the results for the rime ice cases. The case in Fig. 16 is for a velocity of 100 mph and a temperature of 0°F. The case in Fig. 17 is for a velocity of 200 mph and a temperature of 0°F. Both cases show the same trend as in the glaze and mixed ice cases with the density values near 0.917 g/cm^3, with small deviations due to nonuniformities in the x-ray beam and the thickness of the ice sample, and with large density variations due to the presence of voids in the ice. There are no major changes in the density when the densities are measured along a line that crosses from one region with a given morphology to another of a different morphology; dramatic changes in the density seem to come only from the presence of air pockets in the ice.

D. Total Density Measurements

Table 3 lists the total density measurements. For all cases, the total density measured approaches 0.880 g/cm^3.

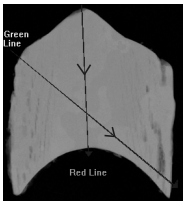

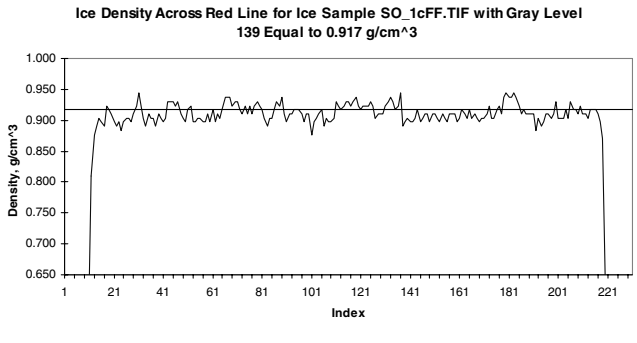

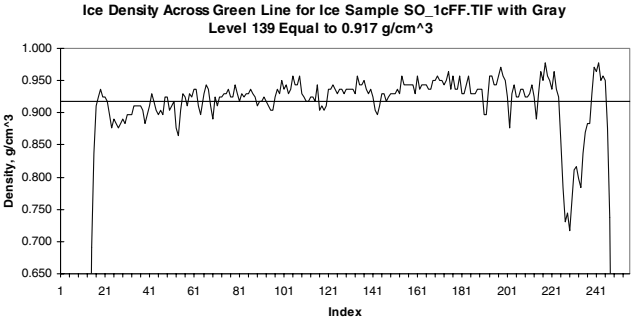

Fig. 14 Sample $SO_{1cFF.TIF}$ for the mixed ice case $V = 150$ mph, LWC $= 0.75$ g/m^3, MVD $= 20$ μm, $T_{tot} = 12°$F, and $\tau = 12$ min.

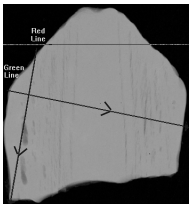

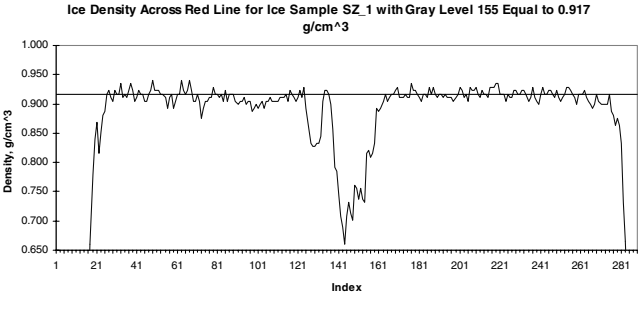

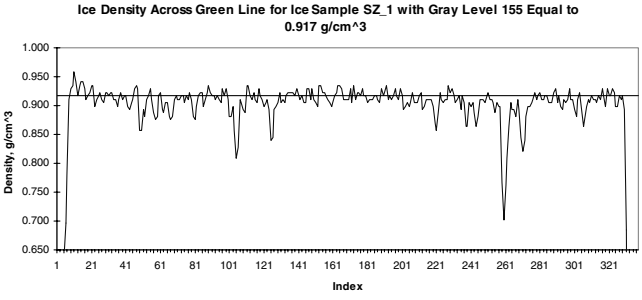

Fig. 15 Sample $SZ_{1cFF.TIF}$ for the mixed ice case $V = 150$ mph, LWC $= 1.0$ g/m^3, MVD $= 30$ μm, $T_{tot} = 0°$F, and $\tau = 12$ min.

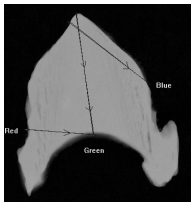

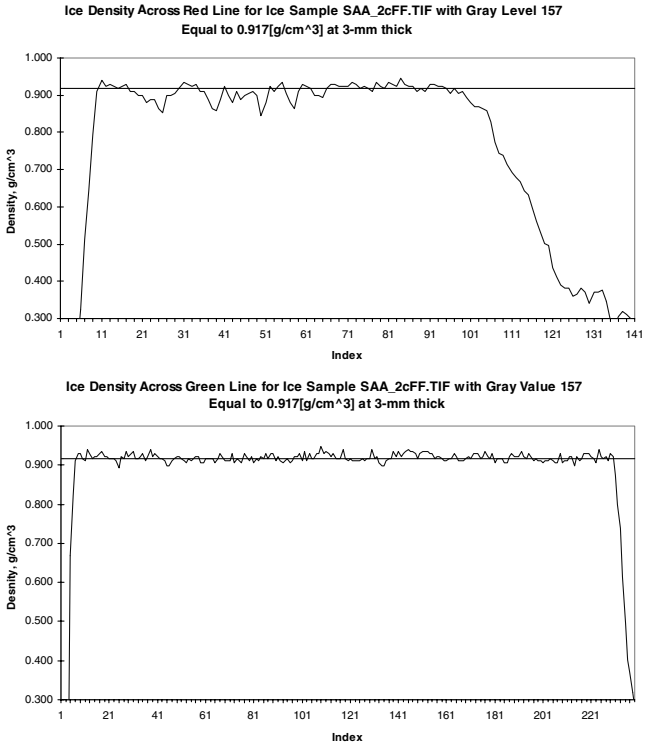

Fig. 16 Sample $SAA_{2cFF.TIF}$ for the rime ice case. No data are presented for the line labeled Blue. $V = 100$ mph, LWC $= 1.0$ g/m^3, MVD $= 20$ μm, $T_{tot} = 0°$F, and $\tau = 12$ min.

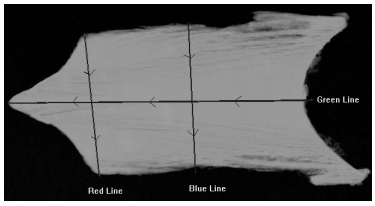

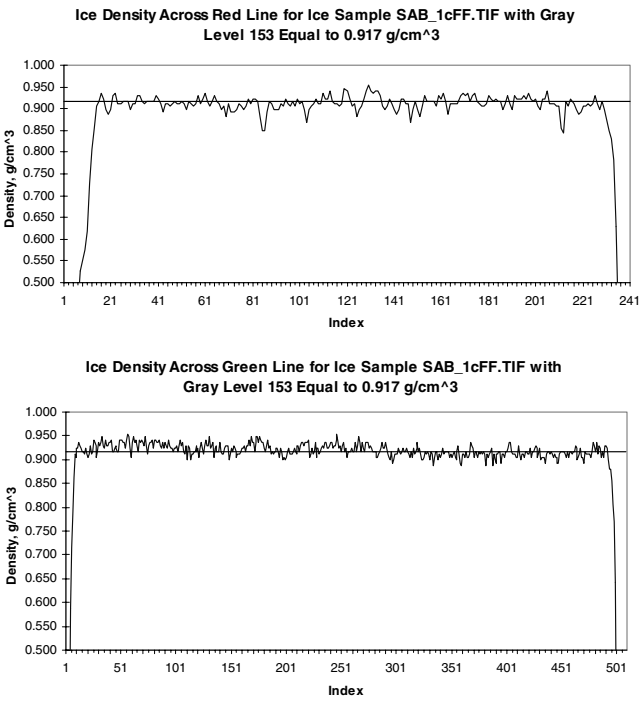

Fig. 17 Sample $SAB_{1cFF.TIF}$ for the rime ice case. No data are presented for the line labeled Blue. $V = 200$ mph, LWC $= 1.0$ g/m^3, MVD $= 20$ μm, $T_{tot} = 0°$F, and $\tau = 12$ min.

E. Comments on Density Measurement Results

The values of the measured total densities for glaze, mixed, and rime ice cases were very close. For the local densities, the main cause of changes in the local values was the presence of air pockets. In areas in which there were no air pockets, the local density for the mixed and rime ice cases approached the value measured for glaze ice. The high value of the density in the rime ice areas can be attributed to the high velocity (greater than 45 m/s) of the supercooled droplets deforming and freezing on impact. Although enough air is trapped by the impacting supercooled droplets to give the rime ice areas the typical whitish appearance, the amount of trapped air is not enough to make an appreciable difference in the value of the density.

V. Conclusions

Local and total density measurements have been performed on ice shapes accreted on a NACA 0012 airfoil mounted vertically in the Icing Research Tunnel at a 0-deg angle of attack. The ice shapes were accreted for a range of icing conditions chosen to produce glaze, mixed, and rime ice accretions. The density measurements show that for all cases, the local densities tend to the approximate value of 0.917 g/cm^3, with small deviations due to nonuniformities in the x-ray beam and small variations in the thickness of the sample. Large variations in density were due to air pockets in the ice samples. The density does not change significantly when the morphology of the ice changes, only when there are air pockets present.

All glaze ice shapes studied show the presence of air pockets. The presence of air pockets in ice shapes had also been observed by Olsen

Table 3 Total density

Image	Average gray value	Reference gray value	Total density, g/cm^3	Approximate measured thickness, in.	Ice type
$SAG_{2cFF.TIF}$	152.68	156.47	0.895	0.118	glaze
$SAH_{2cFF.TIF}$	142.95	150.73	0.870	0.118	glaze
$SAI_{1cFF.TIF}$	146.55	154.41	0.870	0.118	glaze
$SAO_{1cFF.TIF}$	147.51	157.90	0.857	0.121	glaze
$SAM_{1cFF.TIF}$	145.91	148.01	0.904	0.118	glaze
$SAL_{1cFF.TIF}$	140.78	148.69	0.868	0.117	glaze
$SR_{1cFF.TIF}$	147.15	156.53	0.862	0.118	glaze
$SAJ_{1cFF.TIF}$	149.81	158.83	0.865	0.119	mixed
$SL_{1cFF.TIF}$	135.38	142.11	0.874	0.116	mixed
$SO_{1cFF.TIF}$	136.81	139.22	0.901	0.109	mixed
$SN_{2cFF.TIF}$	143.01	147.43	0.890	0.118	mixed
$SS_{1cFF.TIF}$	150.25	155.00	0.889	0.118	mixed
$SZ_{1cFF.TIF}$	151.60	154.56	0.899	0.118	mixed
$SAB_{1cFF.TIF}$	145.89	153.22	0.873	0.113	mixed

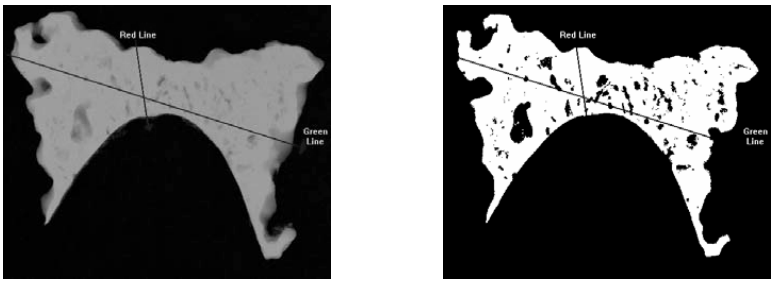

a) Glaze ice case. Sample SAO_1cFF.TIF

V=200 mph, LWC=1.25 g/m^3, MVD=20 μm, T_{tot}= 28 °F, τ= 12 min

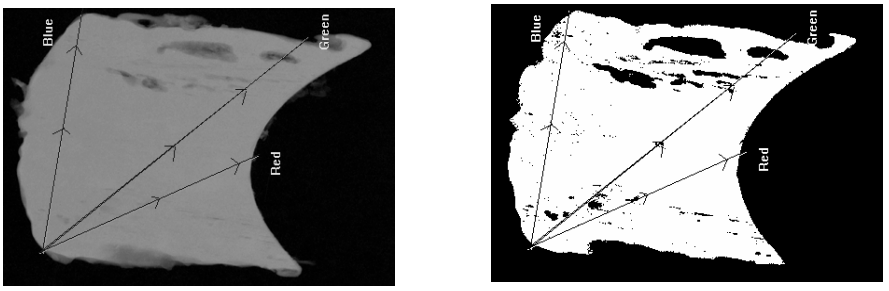

b) Mixed ice case. Sample SL_1cFF.TIF

V=150 mph, LWC=1.0 g/m^3, MVD=20 μm, T_{tot}= 12 °F, τ= 12 min

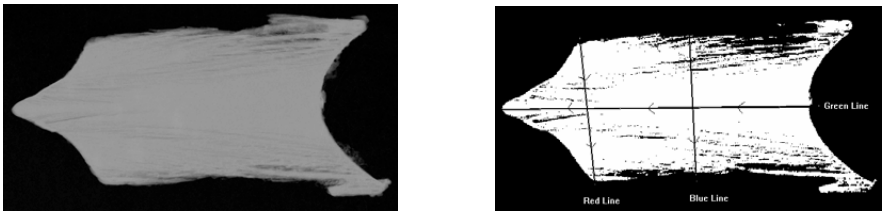

c) Rime ice case. Sample SAB_1cFF.TIF

V=200 mph, LWC=1.0 g/m^3, MVD=20 μm, T_{tot}= 0 °F, τ= 12 min

Fig. 18 Air pockets in glaze, mixed, and rime ice shapes. For each case, the original image (left side) has been enhanced (right side) using Adobe Photoshop to show the presence of air pockets.

and Walker , although the frequency of occurrence was not expected to be this high. Mixed and rime ice shapes also showed the presence of air pockets, although they occur less frequently in these cases than in the glaze ice cases. Figure 18 illustrates the air pockets present in glaze, mixed, and rime ice. The observation of air pockets in ice shapes is important when comparing the predictions from ice accretion codes against actual ice shapes, because the presence of the air pockets will require less mass for a given ice accretion shape.

The experiment presented has shown that Prodi's methodology, augmented with modern imaging techniques, allows the measurement of local and total densities in ice shapes accreted on airfoils. Improvements in the accuracy of the technique can be achieved by using a higher-quality x-ray source to obtain a better uniformity of the beam, and improvements in the microtoming technique would allow ice samples to be obtained with more uniform thickness.

Appendix: Use of a Separate Reference Piece to Improve Accuracy

In the results presented for this experiment, the reference gray level density D_A was obtained in a region of the ice sample that was clear of bubbles and had a thickness close to 3 mm. A better and more accurate approach would have been to use a separate reference piece. A reference piece can be made by freezing very clean water in a medium-sized container, the resulting ice will show some bubbles in the middle, but will be away from the middle zone. The ice can be sawed to a thin slice, and pieces of clear ice can be cut to be used as reference pieces. These pieces can be microtomed to the desired thickness.

Although the thickness of the reference piece needs to be known accurately, in principle, it does not need to be the same thickness as the ice sample for which local densities are being measured. If a reference piece of thickness X_R is x-rayed next to an ice sample of different thickness X_A, and if D_R is the measured photographic density for the reference piece of thickness X_R, then the measured photographic density that would be obtained for a reference piece of thickness X_A can be calculated from Eq. (15) in the following way:

$$X_R/X_A = (D_o - D_R)/(D_o - D_A) \tag{A1}$$

where D_R is the measured photographic density in the region of the reference piece of thickness X_R, D_o is the measured photographic density in the region of the film clear of the reference piece, and D_A is the calculated measured photographic density in the region of the reference piece if it were of thickness X_A. Knowing the thickness and the measured photographic density of a reference piece in a given radiograph, the measured photographic density for any other thickness can be calculated.

If an ice sample has parallel top and bottom surfaces with thickness X_A, we can calculate local densities using a reference piece of known X_R and D_R. D_A is calculated from the reference piece with Eq. (A1) and used in Eq. (16) to calculate the local densities.

If the ice sample does not have parallel surfaces, but we know the thickness of the ice sample at the locations for which the densities are needed, Eq. (A1) can be used to calculate the D_A at each location, and then Eq. (16) can be used to calculate the densities.

Either having an ice sample with parallel top and bottom surfaces or knowing the thickness at the locations for which the density

measurements are wanted, the densities can be calculated with the help of a reference piece of known thickness and measured photographic density.

Acknowledgments

The authors would like to thank William Sexton, Dave Sheldon, and all the personnel at the NASA John H. Glenn Icing Research Tunnel for their help in all phases of the experiment. Special thanks to Clark Hahn for sharing his expertise in x-ray imaging and for his participation in the experiment. We would also like to thank Gary Nolan and Janet Ivancic for their assistance in the digital imaging portions of the experiment, Colin Bidwell for his participation in the initial planning stages of the experiment, and Andrew Reehorst for his help in suggesting a technique to measure local ice densities.

References

[1] Prodi, F., "Measurements of Local Density in Artificial and Natural Hailstones," *Journal of Applied Meteorology*, Vol. 9, Dec. 1970, pp. 903–910.

[2] Prodi, F., "X-Ray Images of Hailstones," *Journal of Applied Meteorology*, Vol. 8, June 1969, pp. 458–459.

[3] Jones, K. F., "The Density of Natural Ice Accretions Related to Non-Dimensional Icing Parameters," *Quarterly Journal of the Royal Meteorological Society*, Vol. 116, 1990, pp. 477–496.

[4] Macklin, W. C., "The Density and Structure of Ice Formed by Accretion," *Quarterly Journal of the Royal Meteorological Society*, Vol. 88, 1962, pp. 30–50.

[5] Rios, M. A., "Icing Simulations Using Jones' Density Formula for Accreted Ice and LEWICE," AAIA Paper 1991-556, Jan. 1991.

[6] Soeder, R. H., Sheldon, D. W., Andracchio, C. R., and Ide, R. F., "NASA Lewis Icing Research Tunnel User Manual," NASA TM-107159, June 1996.

[7] Adobe Photoshop, Software Package, Ver. 3.0, Adobe Systems Inc., San Jose, CA, 1994.

[8] Sigma Scan/Image, Software Package, Ver. 1.20.09, SPSS, Inc., (formerly Jandel Scientific Corp.), Chicago, IL, 1993.

[9] Microsoft Excel, Software Package, Ver. 5.0, Microsoft Corp., Seattle, WA, 1994.

[10] Olsen, W., and Walker, E., "Experimental Evidence for Modifying the Current Physical Model for Ice Accretion on Aircraft Surfaces," NASA TM-87184, May 1986.